Structure versus properties in -Fe_2O_3 nanowires and nanoblades

2016 Nanotechnology 27 035702

(http://iopscience.iop.org/0957-4484/27/3/035702)

IOP Publishing Nanotechnology
Nanotechnology 27 (2016) 035702 (7pp) doi:10.1088/0957-4484/27/3/035702

Structure versus properties in α-Fe_2O_3 nanowires and nanoblades

Chao Wang[1], Yiqian Wang[1], Xuehua Liu[1], Huaiwen Yang[2], Jirong Sun[2], Lu Yuan[3], Guangwen Zhou[3] and Federico Rosei[4]

[1] The Cultivation Base for State Key Laboratory & College of Physics, Qingdao University, No. 308 Ningxia Road, Qingdao 266071, People's Republic of China
[2] Sate Key Laboratory of Magnetism and Beijing National Laboratory for Condensed Matter Physics, Institute of Physics, Chinese Academy of Sciences, Beijing 100080, People's Republic of China
[3] Department of Mechanical Engineering & Multidisciplinary Program in Materials Science and Engineering, State University of New York, Binghamton, NY 13902, USA
[4] Centre Energie, Matériaux et Télécommunications, Institut National de la Recherche Scientifique, 1650 Boulevard Lionel-Bvvvoulet, Varennes, Québec, J3X 1S2, Canada

E-mail: yqwang@qdu.edu.cn

Received 9 October 2015
Accepted for publication 5 November 2015
Published 4 December 2015

Abstract

We report structure/property relationships in bicrystalline α-Fe_2O_3 nanowires (NWs) and nanoblades (NBs), synthesized by thermal oxidation of iron foils with different surface roughness. The electrical properties of individual nanostructures were studied by *in situ* transmission electron microscopy. Current–voltage (*I–V*) measurements using gold electrodes showed that a Schottky contact forms between α-Fe_2O_3 NWs whereas an ohmic contact forms between α-Fe_2O_3 NBs. The difference in transport properties is attributed to the existence of oxygen vacancies in the coincidence-site-lattice boundary region of α-Fe_2O_3 NBs. Magnetic measurements indicate that the temperature-dependent zero-field-cooled magnetization rises more rapidly near the Morin transition temperature for α-Fe_2O_3 NBs than that for NWs. The distinct magnetic properties of the NBs are ascribed to the enhanced magnetic order induced by the structural order in the two-dimensional NBs. These α-Fe_2O_3 NBs are promising building blocks for electronic and magnetic devices since their 2D geometries facilitate integration into devices with realistic pathways to manufacturing. In addition, our study shows that boundary engineering is an effective approach for tailoring the physical properties of nanomaterials.

Keywords: one-dimensional Fe_2O_3 nanowires, two-dimensional Fe_2O_3 nanoblades, grain boundary, electrical properties, magnetic properties

(Some figures may appear in colour only in the online journal)

1. Introduction

The physical and chemical properties of nanomaterials strongly depend on their size, shape, and dimensionality [1, 2]. In addition to the atomic scale structure, crystal defects such as atomic vacancies and grain boundaries also have a great impact on the properties of nanomaterials [3–5]. Material scientists usually prefer defect-free structures in their pursuit to make predictable devices with high performance. Defects are thus perceived as material imperfections which could adversely affect device performance. However, because of the limited size of nanomaterials, the presence of defects can in fact be effectively used to regulate their local properties and achieve new functionalities towards the realization of novel devices. In bulk materials, defects such as grain boundaries have been extensively studied for many decades, especially in the contexts of mechanical strength and ductility of metals [6, 7]. However, because grain boundaries in small volume nanomaterials are scarce and the corresponding property measurements are challenging, limited studies have been reported so far.

Hematite (α-Fe_2O_3) has been widely studied because of its nontoxicity, low cost, high stability under ambient conditions, and multifunctionality [8]. Hematite has been intensively investigated for applications in lithium-ion batteries [9, 10], sensors [11, 12], catalysts [13] and magnetic devices [14]. The performance of α-Fe_2O_3 is greatly influenced by its dimensionality, morphology, and microstructure. In our previous studies, different types of α-Fe_2O_3 nanostructures including bicrystalline 1D α-Fe_2O_3 nanowires (NWs)[8] and 2D nanoblades (NBs)[9,] were synthesized, and their optical properties were also investigated. It is found that the optical properties show a clear dependence on the growth morphologies of the nanostructured hematite.

Here we study structure versus properties in α-Fe_2O_3 nanostructures, comparing NWs and NBs. We focus on the investigation of electrical and magnetic properties and find that there are significant changes associated with different nanoscale structures. The measured *I–V* curve from the α-Fe_2O_3 NW is nonlinear and almost symmetrical, leading to a Schottky contact at the interfaces between semiconducting NWs and two gold electrodes. On the other hand, the measured *I–V* curve for the α-Fe_2O_3 NB exhibits an obviously linear *I–V* relationship, indicating that an ohmic contact forms between the α-Fe_2O_3 NB and gold electrodes. The difference in transport properties is attributed to the existence of oxygen vacancies which increase the carrier concentration in the n-type semiconductor. Magnetic measurements show that near the Morin transition temperature the temperature dependent zero-field-cooled magnetization rises more rapidly for α-Fe_2O_3 NBs than that for NWs. The distinct magnetic properties of the NBs are ascribed to the enhanced magnetic order induced by the structural order in the two-dimensional nanosheets.

2. Experimental section

The detailed synthesis procedure of α-Fe_2O_3 NWs and NBs was reported elsewhere [15, 16]. Specimens for transmission electron microscopy (TEM) observations were prepared by peeling off the black products from the surface of oxidized Fe foils, then ultrasonicating them in ethanol for two minutes and dispersing a drop onto a holey-carbon-film-coated copper grid. Bright field (BF), selected-area electron diffraction (SAED), high-resolution TEM (HRTEM) and electron energy-loss spectroscopy (EELS) were carried out using field-emission TEMs (JEOL JEM 2100F or FEI Tecnai F20) operated at 200 kV. All EELS spectra were acquired in image mode with an electron beam probe size of 1 to 2 nm and a half collection angle of ~16 mrad with an acquisition time of 2 s.

The electrical properties of individual NWs and NBs were investigated using an *in situ* TEM sample holder (FM200E HA300) purchased from Sweden Nanofactory Company, specially designed to measure the electrical properties of nanomaterials. Specimens were dispersed onto the tip of a gold rod on the holder that was moved to touch an atomic force microscopy cantilever, also made of gold, using a piezo-driven manipulator inside the TEM. The applied bias voltage ranged from −5.0 V to 5.0 V. A schematic diagram for *in situ* measurement of electrical properties is shown in figure 1. The magnetic properties of NWs and NBs were studied using a Quantum Design superconducting quantum interference device (SQUID, Quantum Design, MPMS VSM). The temperature-dependent magnetization was measured under an applied magnetic field of 0.01 T. For the measurements of magnetic properties, α-Fe_2O_3 NWs and NBs were first peeled off from Fe substrates and then attached to the outer surface of a glass rod in the MPMS apparatus.

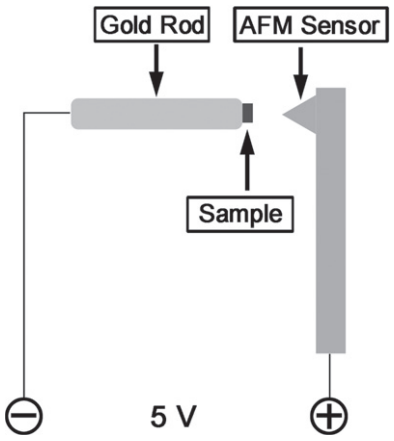

Figure 1. Schematic diagram for *in situ* measurement of electrical property.

3. Results and discussion

Figures 2(a) and (b) are typical cross-sectional SEM and TEM images of the oxidized products, showing that α-Fe_2O_3 NWs cover the entire surface of the oxidized Fe foil. Figure 2(c) is a representative BF TEM image of an individual bicrystalline α-Fe_2O_3 nanowire (NW) with a diameter of ~43 nm. The inset in figure 2(c) shows that the bicrystal interface is parallel to its length direction. A twin boundary is clearly visible in the HRTEM image (figure 2(d)). From the analysis of the associated SAED pattern (figure 2(e)) two sets of diffraction spots can be identified, one being the [0001] zone-axis labeled by red lines, and the other being the $[1\bar{1}0\bar{1}]$ zone-axis marked by yellow lines.

Figure 3(a) shows a typical cross-sectional SEM image of α-Fe_2O_3 NBs. These NBs are formed through the coalescence of two nanoscale islands during the oxidation process, possessing a bicrystal structure. Figure 3(b) shows cross-sectional TEM image of the NBs with dimensions of about 1 μm long and 500 nm wide. Figure 3(c) displays a BF TEM image of an individual α-Fe_2O_3 NB. Careful examination of the NB edge in the inset of figure 3(c) shows that it is not a single layer, but rather a double-layered structure. In figure 3(d) we report a typical [0001] zone-axis HRTEM image from the α-Fe_2O_3 NB edge. The image shows two parts, the lower part being a single-layered lattice image of α-Fe_2O_3, and the upper part being Moiré fringe contrast formed by the overlap of double-layered α-Fe_2O_3 crystal lattices.

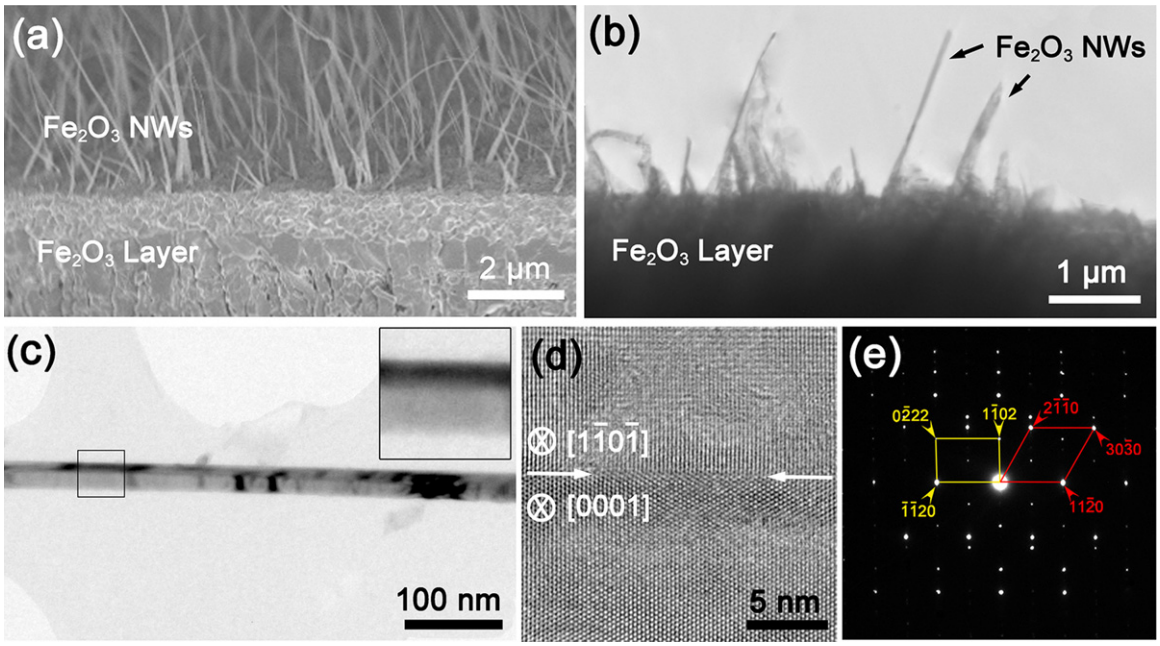

Figure 2. Cross-sectional SEM image (a) and TEM image (b) of bicrystalline α-Fe_2O_3 NWs; (c) TEM image of individual bicrystalline α-Fe_2O_3 NW; typical HRTEM image (d) and SAED pattern (e) taken from the α-Fe_2O_3 NW in (c).

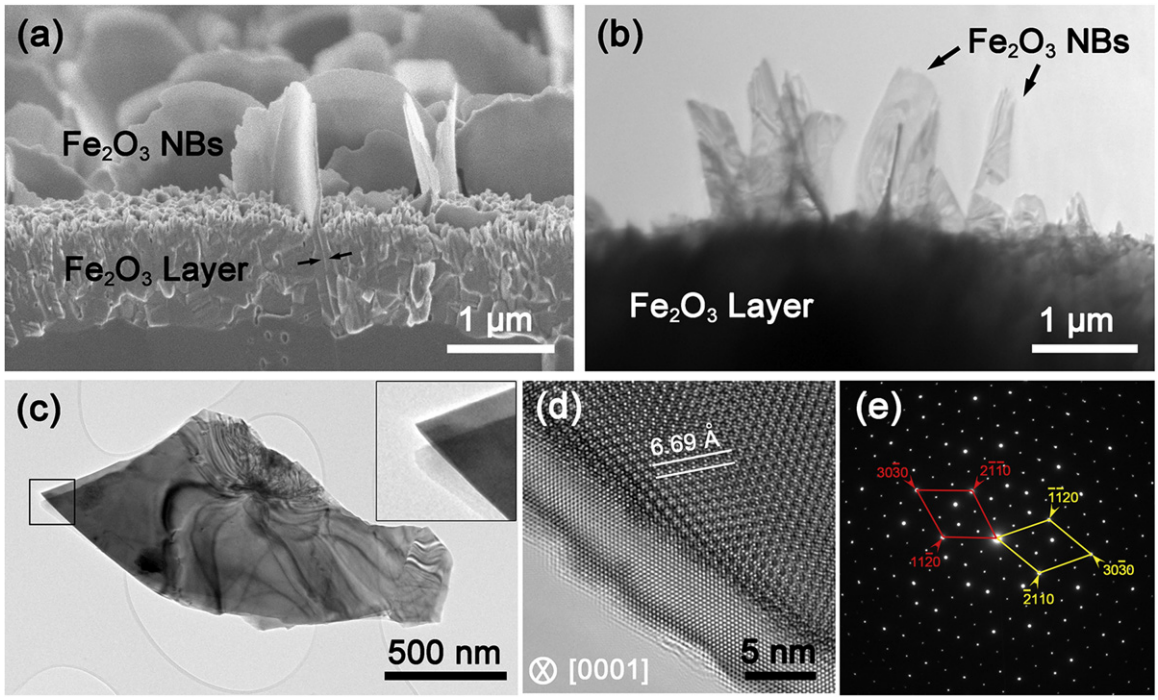

Figure 3. Cross-sectional SEM image (a) and TEM image (b) of bicrystalline α-Fe_2O_3 NBs; (c) TEM image of individual bicrystalline α-Fe_2O_3 NB; typical HRTEM image (d) and SAED pattern (e) taken from the α-Fe_2O_3 NB in (c).

Figure 3(e) is a SAED pattern taken from the α-Fe_2O_3 NB in figure 3(c), containing two sets of [0001] zone-axis diffraction spots which can be indexed using the lattice parameters of α-Fe_2O_3. These two sets of diffraction spots are rotated with respect to each other by an angle of 21.79°, indicating this is a typical coincidence-site-lattice (CSL) boundary [17, 18]. Comparison with the literature [17, 18] shows that this CSL boundary has a Σ value of 13. Both α-Fe_2O_3 NWs and NBs have a bicrystalline structure. However, their interfaces are intrinsically different. Bicrystalline NWs have a twinning structure which generates a coherent boundary with few defects, while bicrystalline NBs exhibit a large-angle twist boundary. Such dissimilar interfacial configurations may lead to different electronic structures.

To analyze the electronic structure of the α-Fe_2O_3 NWs and NBs, we carried out extensive EELS experiments.

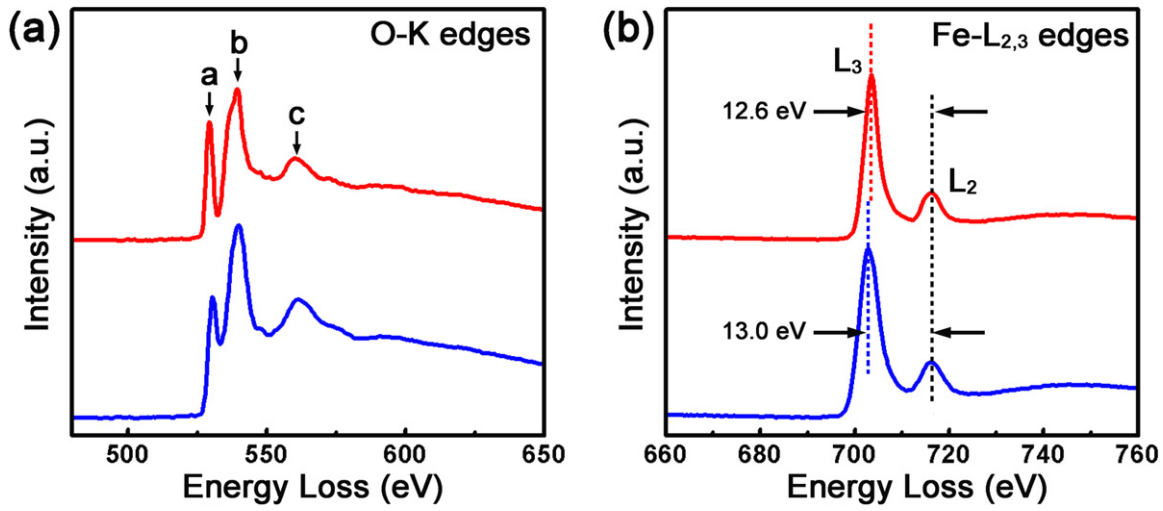

Figure 4. Typical EELS spectra of O-K edges (a) and Fe-$L_{2,3}$ edges (b) acquired from an individual α-Fe_2O_3 NW (red curves) and α-Fe_2O_3 NB (blue curves), respectively.

Figure 4 shows typical EELS spectra of oxygen K-edges and Fe-$L_{2,3}$ edges for an α-Fe_2O_3 NW and NB, respectively. For α-Fe_2O_3 NB, the spectra are collected from the central regions of the sample. In figure 4(a), three peaks (labeled a–c) can be identified in the oxygen K-edge energy-loss near-edge fine structure. Quantification of the EELS spectra in figure 4(a) shows that the intensities of peaks a and b for the NB are lower than those for the NW. It was previously demonstrated that the decreased intensities of these peaks are associated with oxygen vacancies inside the nanostructures [19, 20]. Thus, the lower the peak intensities in the EELS spectra, the higher the content of oxygen vacancies in α-Fe_2O_3. Then, it can be deduced that the content of oxygen vacancies is higher in the α-Fe_2O_3 NBs than in the α-Fe_2O_3 NWs. In addition, the Fe-L edges can provide us with the ionization status of metal cations by determining the relative intensity and position of individual L_3 and L_2 edges, respectively [20]. The Fe $L_{2,3}$ edges spectra for α-Fe_2O_3 NW and NB are shown in figure 4(b). The quantification of the EELS spectra in figure 4(b) shows that the intensity ratio I(L_3)/I(L_2) is 5.1 ± 0.3 for the α-Fe_2O_3 NW and 4.2 ± 0.3 for the α-Fe_2O_3 NBs. In addition, the separation between the L_2 and L_3 lines remains constant (~12.6 eV) for the α-Fe_2O_3 NW, however, chemical shifts of L_3 line of about 0.4 eV for the NB are detected. It was reported that the intensity ratio I(L_3)/I(L_2) and the position of the L_3 line are sensitive to the valance states of the transition metal oxides [11]. As a result, the significant decrease in the intensity ratio I(L_3)/I(L_2) and chemical shifts for the L_3 lines indicate a change in the partial oxidation states from Fe^{3+} to Fe^{2+}, consistent with other reports [11]. In addition, quantification of the EELS spectra shows that the atomic ratios of Fe and O are 2:(3.00 ± 0.03) for the α-Fe_2O_3 NW, and 2:(2.92 ± 0.02) for the α-Fe_2O_3 NB, respectively. Thus, it can be concluded that more oxygen vacancies exist in NBs than in NWs.

To investigate the influence of boundary configurations on the electrical properties of the α-Fe_2O_3 nanostructures, the electrical behavior of individual α-Fe_2O_3 NW and NB was studied by *in situ* TEM. To obtain a reliable and statistically relevant experimental result, more than 10 individual α-Fe_2O_3 NWs and NBs were examined. Under TEM inspection the nanomanipulator probe electrode was carefully adjusted to touch the samples, as shown in figures 5(a) and (c). A metal-semiconductor contact can be either a Schottky contact or an ohmic contact depending on the Fermi surface alignment between the metal electrode and the semiconductor [21, 22]. Figure 5(b) reports the measured *I–V* curve from the α-Fe_2O_3 NW, which is nonlinear and almost symmetrical. No current is detected between bias voltages from −0.8 V to 0.8 V, and a rapid current increase appears beyond this bias range. Such threshold effect may be ascribed to two Schottky contacts formed at the interfaces of the semiconducting NW and two gold electrodes [23, 24]. However, the measured *I–V* curve for the α-Fe_2O_3 NB in figure 5(d) exhibits an obviously linear *I–V* relation, indicating that an ohmic contact forms between the α-Fe_2O_3 NB and gold electrodes. The resistance of α-Fe_2O_3 NB can be estimated directly from the linear *I–V* curve, whereas the resistance of α-Fe_2O_3 NW can only be obtained from the large bias region in the *I–V* curve since the total voltage at the low bias is mainly controlled by the two Schottky barriers [23]. The resistivity of α-Fe_2O_3 NB and NW can be determined by

$$\rho = \frac{SR}{L}, \tag{1}$$

where R is the resistance, and S and L are the cross-sectional area and length of the sample, respectively. We found that the resistivity of the NB is $\sim 6.9 \times 10^{-3}\,\Omega\,\mathrm{m}$, smaller by three orders of magnitude than that of the NW ($\sim 4.1\,\Omega\,\mathrm{m}$).

The α-Fe_2O_3 NWs synthesized in oxidative ambient at high temperature are p-type semiconductors [25]. The work function of Au ($\phi_M = 5.1$ eV) is slightly smaller than that of α-Fe_2O_3 NWs ($\phi_S = 5.4$ eV) [26]. In the schematic band diagram shown in figure 6(a), the Fermi level of α-Fe_2O_3 is lower than that of Au, leading to band bending when Au contacts α-Fe_2O_3. Therefore, a Schottky barrier will form

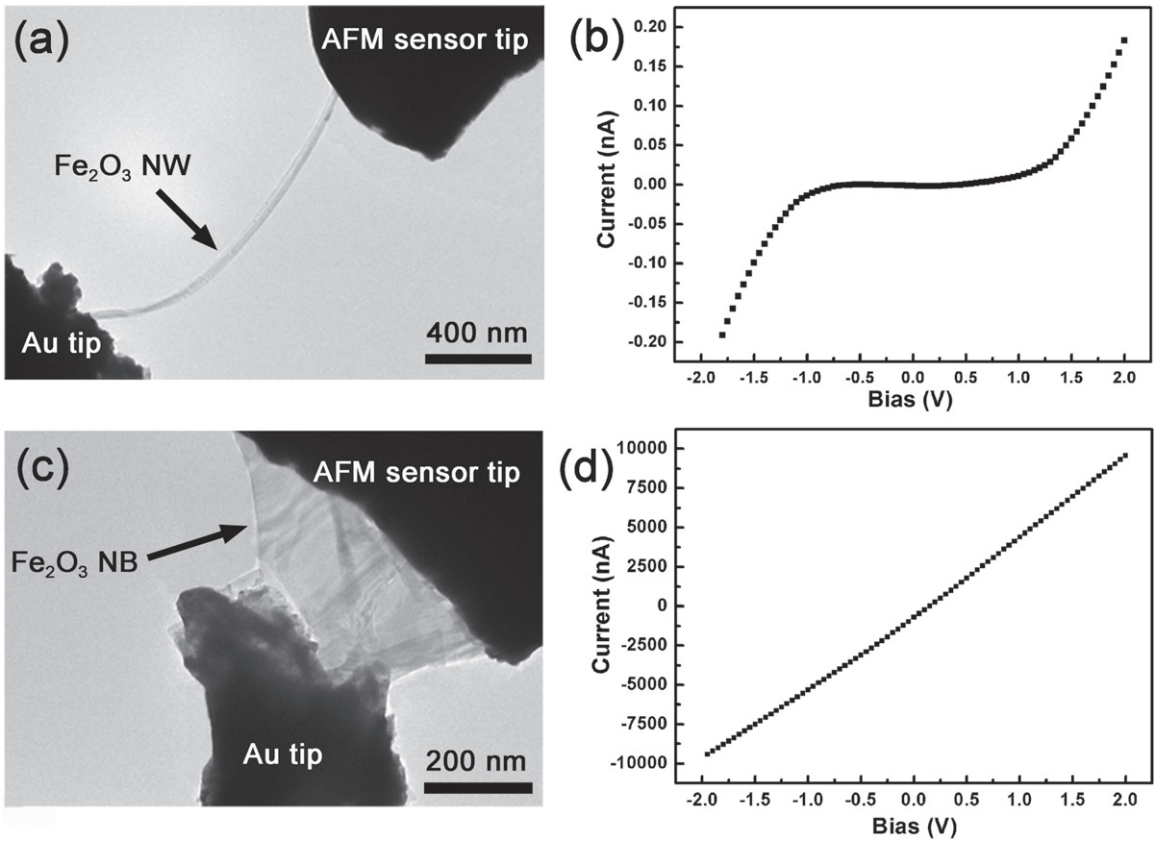

Figure 5. Typical BF TEM images of single α-Fe_2O_3 NW (a) and α-Fe_2O_3 NB (c) in contact with two gold electrodes; *I–V* curves measured from single α-Fe_2O_3 NW (b) and α-Fe_2O_3 NB with a CSL boundary (d).

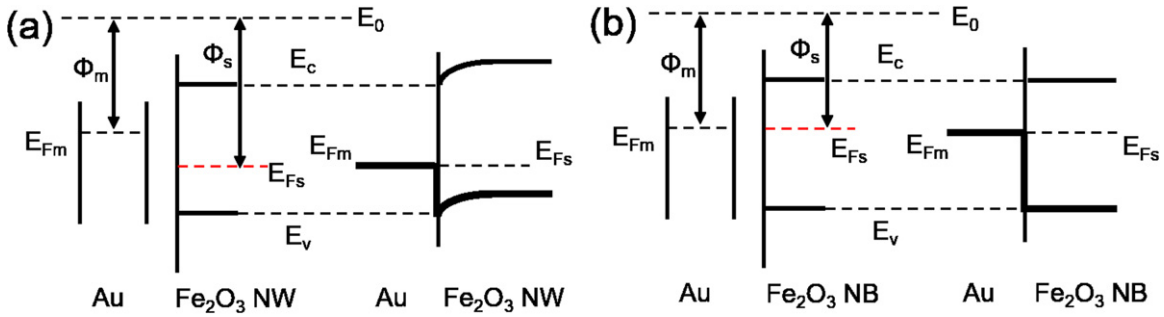

Figure 6. Schematic band diagrams of the contact between Fe_2O_3 NW and Au electrodes (a), between Fe_2O_3 NB and Au electrodes (b).

between Au and α-Fe_2O_3 NWs. It has been demonstrated that α-Fe_2O_3 undergoes a peculiar transition from p-type to n-type under certain conditions due to its small bandgap ($E_g = 2.2$ eV) [26]. The α-Fe_2O_3 NBs examined by *in situ* TEM have an n-type nature as a result of oxygen deficiencies in the CSL boundary region. The oxygen vacancies in the CSL boundary region of the α-Fe_2O_3 NB may result in a change in the work function. The Fermi level of the Fe_2O_3 NB shifts readily towards the conduction band (E_c) (figure 6(b)), and thus the work function of the Fe_2O_3 NB decreases to be smaller than that of Fe_2O_3 NW. In the schematic band diagram (figure 6(b)), the Fermi levels of Fe_2O_3 NB and Au are aligned, yielding an ohmic contact. Therefore, the *I–V* characteristic of α-Fe_2O_3 NB exhibits a linear relation. In addition, the oxygen vacancies increase the carrier concentration in the n-type semiconductor, which enhances the electrical performance of the α-Fe_2O_3 NBs.

A magnetic phase transition from a canted ferromagnetic phase to an antiferromagnetically ordered state at ~264 K has been reported for bulk hematite [27]. This transition is characterized by a sharp decrease in the zero-field cooling (ZFC) and field cooling (FC) magnetization curves called a Morin transition. Figure 7 shows the temperature dependence of ZFC and FC magnetization for α-Fe_2O_3 NWs and NBs. Both the NWs and the NBs exhibit a well-defined peak at 122 K, which corresponds to the Morin transition. The Morin

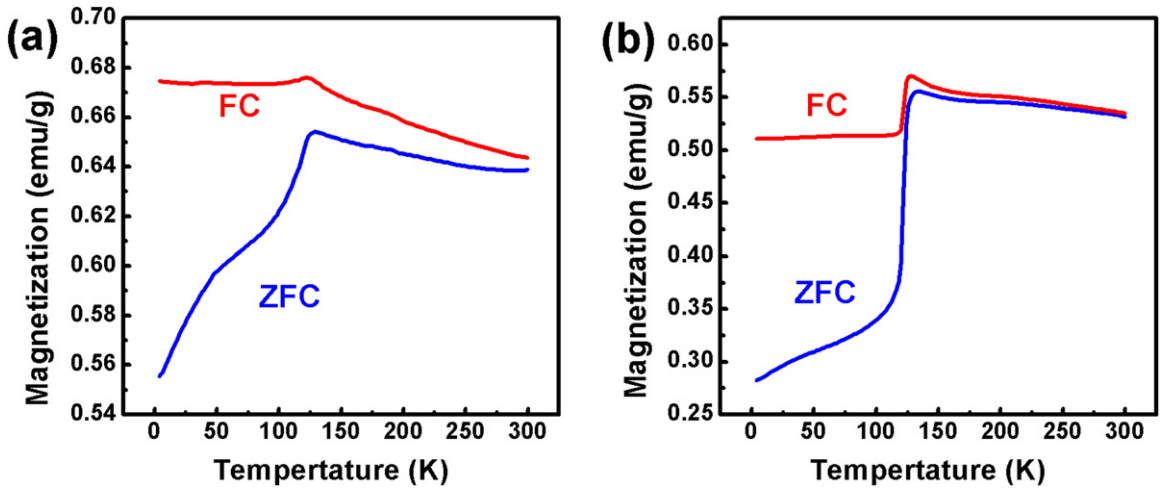

Figure 7. Temperature dependence of ZFC and FC magnetization for α-Fe_2O_3 NWs (a) and NBs (b) at an applied field of 0.01 T.

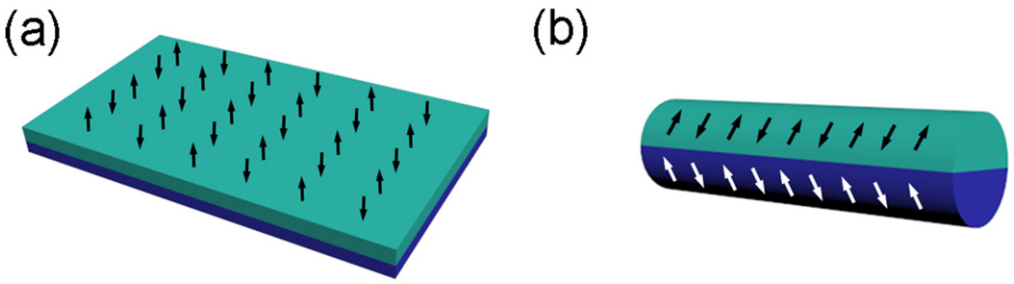

Figure 8. Schematic diagram of spin arrangements in Fe_2O_3 NB (a) and Fe_2O_3 NW (b) when T is lower than 122 K.

temperature of the α-Fe_2O_3 nanostructure decreases with decreasing size. The magnetic behavior of our α-Fe_2O_3 NWs is consistent with the expected behavior of hematite [28]. However, the α-Fe_2O_3 NBs show an obviously different magnetic behavior. The magnetization curve of the NBs rises more sharply than that of NWs near this Morin transition temperature. Since no secondary phases are detected in our samples, the magnetic behavior observed here is ascribed to an intrinsic property.

Considering the dimensionality and orientation relationship change of these α-Fe_2O_3 nanostructures, we ascribe their different magnetic behaviors to an enhanced magnetic ordering accompanied by the interfacial structural order in the 2D α-Fe_2O_3 NBs. Above the Morin temperature, α-Fe_2O_3 is a canted antiferromagnet with spins perpendicular to the c-axis except for a slight canting about 1 min of arc out of the basal plane [29]. When the temperature is decreased to 122 K, α-Fe_2O_3 is a uniaxial antiferromagnet with spins lying along the c-axis and the magnetic moments in α-Fe_2O_3 are frozen or blocked [30]. In our experiment, bicrystalline α-Fe_2O_3 NBs have a unified direction of the c-axis as shown in figure 3(d), while the direction of the c-axis in bicrystalline α-Fe_2O_3 NW is not uniform as shown in figure 2(d). Below 122 K, the magnetic moments in the 2D α-Fe_2O_3 NBs are more ordered than those in the 1D α-Fe_2O_3 NWs (figure 8). Therefore, compared with the magnetization curve of α-Fe_2O_3 NW, the ZFC magnetization curve of α-Fe_2O_3 NB shows more drastic changes.

4. Conclusions and perspectives

In summary, bicrystalline 1D α-Fe_2O_3 NWs and 2D α-Fe_2O_3 NBs were synthesized by thermal oxidation of Fe foils. The measured I–V curves show that a Schottky contact forms between α-Fe_2O_3 NW and gold electrodes, whereas an Ohmic contact was created between α-Fe_2O_3 NB and gold electrodes. Such transformation is caused by the special CSL boundary in the α-Fe_2O_3 NB. The magnetic measurements demonstrate that the ZFC magnetization curve of the NBs rises more rapidly near the Morin transition temperature than that of the NWs. Such distinct differences are ascribed to the fact that the magnetic moments in the 2D α-Fe_2O_3 NBs are more ordered than those in the 1D α-Fe_2O_3 NWs. The presence of grain boundaries opens new possibilities in the case of nanostructures since their properties are related to the reduced dimensionality. Understanding and controlling boundary properties in low-dimensional structures will pave the way for tailoring nanomaterial properties in the future.

Acknowledgments

The authors would like to acknowledge financial support from the National Key Basic Research Development Program of China (Grant no.: 2012CB722705), the Natural Science Foundation for Outstanding Young Scientists in Shandong Province, China (Grant no.: JQ201002), and the Program for Foreign

Cultural and Educational Experts (Grant no.: W20123702083, GDW20133400112, GDW20143500163). Y Q Wang would also like to acknowledge financial support from the Top-notch Innovative Talent Program of Qingdao City (Grant no.: 13-CX-8), and the Taishan Scholar Program of Shandong Province, China. F R is grateful to NSERC for an EWR Steacie Memorial Fellowship and for a Discovery Grant.

References

[1] Burda C, Chen X, Narayanan R and El-Sayed M A 2005 Chemistry and properties of nanocrystals of different shapes *Chem. Rev.* **105** 1025

[2] Mokari T, Zhang M and Yang P 2007 Shape, size, and assembly control of PbTe nanocrystals *J. Am. Chem. Soc.* **129** 9864

[3] Ovid'ko I A and Sheinerman A G 2009 Enhanced ductility of nanomaterials through optimization of grain boundary sliding and diffusion processes *Acta Mater.* **57** 2217

[4] Anand B, Krishnan S, Podila R, Sai S S S, Rao A M and Philip R 2014 The role of defects in the nonlinear optical absorption behavior of carbon and ZnO nanostructures *Phys. Chem. Chem. Phys.* **16** 8168

[5] Sato Y, Yamamoto T and Ikuhara Y 2007 Atomic structures and electrical properties of ZnO grain boundaries *J. Am. Ceram. Soc.* **90** 337

[6] Kittel C 2005 *Introduction to Solid State Physics* (New York: Wiley)

[7] Lu K, Lu L and Suresh S 2009 Strengthening materials by engineering coherent internal boundaries at the nanoscale *Science* **324** 349

[8] Cornell R M and Schwertmann U 2006 *The Iron Oxides: Structure, Properties, Reactions, Occurrences and Uses* (New York: Wiley)

[9] Jain G, Balasubramanian M and Xu J J 2006 Structural studies of lithium intercalation in a nanocrystalline α-Fe_2O_3 compound *Chem. Mater.* **18** 423

[10] Wu C, Yin P, Zhu X, OuYang C and Xie Y 2006 Synthesis of hematite (α-Fe_2O_3) nanorods: diameter-size and shape effects on their applications in magnetism, lithium ion battery, and gas sensors *J. Phys. Chem.* B **110** 17806

[11] Sun B, Horvat J, Kim H S, Kim W-S, Ahn J and Wang G 2010 Synthesis of mesoporous α-Fe_2O_3 nanostructures for highly sensitive gas sensors and high capacity anode materials in lithium ion batteries *J. Phys. Chem.* C **114** 18753

[12] Gou X, Wang G, Kong X, Wexler D, Horvat J, Yang J and Park J 2008 Flutelike porous hematite nanorods and branched nanostructures: synthesis, characterisation and application for gas-sensing *Chem.-Eur. J.* **14** 5996

[13] Orlandi M, Caramori S, Ronconi F, Bignozzi C A, El Koura Z, Bazzanella N, Meda L and Miotello A 2014 Pulsed-laser deposition of nanostructured iron oxide catalysts for efficient water oxidation *ACS Appl. Mater. Interfaces* **6** 6186

[14] Chou S G, Stutzman P E, Wang S Z, Garboczi E J, Egelhoff W F and Plusquellic D F 2012 High-resolution terahertz optical absorption study of the antiferromagnetic resonance transition in hematite (alpha-Fe_2O_3) *J. Phys. Chem.* C **116** 16161

[15] Yuan L, Wang Y Q, Cai R S, Jiang Q, Wang J B, Li B, Sharma A and Zhou G W 2012 The origin of hematite nanowire growth during the thermal oxidation of iron *Mater. Sci. Eng.* B **177** 327

[16] Yuan L, Cai R S, Jang J I, Zhu W H, Wang C, Wang Y Q and Zhou G W 2013 Morphological transformation of hematite nanostructures during oxidation of iron *Nanoscale* **5** 7581

[17] Kronberg M and Wilson F 1949 Secondary recrystallization in copper *AIME Trans.* **185** 501

[18] Warrington D 1975 The coincidence site lattice (CSL) and grain boundary (DSC) dislocations for the hexagonal lattice *J. Phys. Colloques* **36** 87

[19] Colliex C, Manoubi T and Ortiz C 1991 Electron-energy-loss-spectroscopy near-edge Fine structures in the iron-oxygen system *Phys. Rev.* B **44** 11402

[20] Chueh Y L, Lai M W, Liang J Q, Chou L J and Wang Z L 2006 Systematic study of the growth of aligned arrays of α-Fe_2O_3 and Fe_3O_4 nanowires by a vapor–solid process *Adv. Funct. Mater.* **16** 2243

[21] Louie S G and Cohen M L 1976 Electronic structure of a metal-semiconductor interface *Phys. Rev.* B **13** 2461

[22] Rhoderick E H and Williams R 1988 *Metal-Semiconductor Contacts* (Oxford: Clarendon)

[23] Zhang Z, Yao K, Liu Y, Jin C, Liang X, Chen Q and Peng L M 2007 Quantitative analysis of current–voltage characteristics of semiconducting nanowires: decoupling of contact effects *Adv. Funct. Mater.* **17** 2478

[24] Wang Y G, Zou B S, Wang T H, Wang N, Cai Y, Chan Y F and Zhou S X 2006 *I–V* characteristics of schottky contacts of semiconducting ZnSe nanowires and gold electrodes *Nanotechnology* **17** 2420

[25] Bevan D J M, Shelton J P and Anderson J S 1948 Properties of some simple oxides and spinels at high temperatures *J. Chem. Soc.* 1729

[26] Fan Z, Wen X, Yang S and Lu J G 2005 Controlled p-and n-type doping of Fe_2O_3 nanobelt field effect transistors *Appl. Phys. Lett.* **87** 013113

[27] Morin F J 1950 Magnetic susceptibility of α-Fe_2O_3 and α-Fe_2O_3 with added titanium *Phys. Rev.* **78** 819

[28] Xu R, Yan H, He W, Su Y, Nie J C and He L 2012 Ultrathin α-Fe_2O_3 nanoribbons and their moiré patterns *J. Phys. Chem.* C **116** 6879

[29] Muench G, Arajs S and Matijević E 1985 The morin transition in small α-Fe_2O_3 particles *Phys. Status Solidi* a **92** 187

[30] Zhou H and Wong S S 2008 A facile and mild synthesis of 1D ZnO, CuO, and α-Fe_2O_3 nanostructures and nanostructured arrays *ACS Nano* **2** 944